

## Co-seismic deformation of the 2017 $M_s$ 7.0 Jiuzhaigou Earthquake observed with GaoFen-3 interferometry

Xue Chen<sup>a,b</sup>, Junhuan Peng<sup>a,c</sup>, Mahdi Motagh<sup>d,e</sup>, Yueze Zheng<sup>f</sup>, Mengyao Shi<sup>a</sup>, Honglei Yang<sup>a,c</sup> and Qingren Jia<sup>g</sup>

<sup>a</sup>School of Land Science and Technology, China University of Geosciences, Beijing, China; <sup>b</sup>Department of Geosciences, University of Padua, Padua, Italy; <sup>c</sup>Shanxi Key Laboratory of Resources, Environment and Disaster Monitoring, Jinzhong, China; <sup>d</sup>Department of Geodesy, Section of Remote Sensing, GFZ German Research Centre for Geosciences, Potsdam, Germany; <sup>e</sup>Institute for Photogrammetry and GeoInformation, Leibniz University Hannover, Hannover, Germany; <sup>f</sup>Photogrammetry and Remote Sensing Department, Beijing Institute of Surveying and Mapping, Beijing, China; <sup>g</sup>College of Resources and Civil Engineering, Northeastern University, Shenyang, China

### ABSTRACT

The first application of GaoFen-3 synthetic aperture radar (SAR) interferometry to monitoring co-seismic deformation of an earthquake is presented in this paper. First, two GaoFen-3 SAR images spanning the 2017 surface-wave magnitude ( $M_s$ ) 7.0 Jiuzhaigou earthquake were mosaicked, coregistered and processed into an interferogram with visible fringes. After the removal of severe orbital errors and unwrapping, the co-seismic deformation field is obtained. Finally, the fault parameters and slip distribution are determined based on the deformation field. To evaluate the performance of GaoFen-3 in this case, the interferogram, co-seismic deformation field, derived fault parameters and slip distribution are compared with those derived from Radarsat-2, Sentinel-1A and Advanced Land Observing Satellite-2 (ALOS-2) Phased Array type L-band Synthetic Aperture Radar-2 (PALSAR-2). The comparisons between the deformation field obtained from GaoFen-3 and those obtained from Radarsat-2 and Sentinel-1A show Pearson's correlation coefficient ( $r$ ) values  $> 90\%$ , demonstrating that GaoFen-3 interferometry can measure the co-seismic deformation effectively. The resultant slip model obtained by GaoFen-3 interferometric measurements shows a simple, elliptical pattern of slip, reaching a maximum of approximately 1 m at depths of 10–13 km. The rake angle is almost  $0^\circ$ , which suggests left-lateral strike-slip motion, consistent with previous studies.

### ARTICLE HISTORY

Received 18 September 2019  
Accepted 21 January 2020

## 1. Introduction

GaoFen-3 is a Chinese multi-polarized C-band synthetic aperture radar (SAR) satellite mission launched in August 2016. It operates in 12 imaging modes, such as stripmap, scanSAR, and sliding spotlight modes (Fan et al. 2018), with resolutions ranging from 1 to 500 m and swath widths ranging from 10 to 650 km (Chen et al. 2018). GaoFen-3 is mainly

---

**CONTACT** Junhuan Peng  [pengjunhuan@163.com](mailto:pengjunhuan@163.com)  School of Land Science and Technology, China University of Geosciences, Beijing, China

This article has been corrected with minor changes. These changes do not impact the academic content of the article.

© 2020 Informa UK Limited, trading as Taylor & Francis Group

designed to be used in the fields of ocean surveillance, disaster reduction, water conservancy and meteorology (Liu, Qiu, and Wen 2016).

Similar to other existing SAR systems, GaoFen-3 can provide intensity and phase information. Previous studies on GaoFen-3 apply intensity information mainly in the following three aspects: (1) quantitative inversion, e.g. wave height retrieval (Wang et al. 2018a), wind retrieval (Lei et al. 2018), and soil moisture retrieval (Zhang et al. 2018a); (2) objective detection, e.g. flood detection (Kang et al. 2018), ship detection (Hao et al. 2018), and coastline detection (Meng et al. 2018); and (3) land cover classification combining optical images (Fang et al. 2018). For the phase information, Zhang et al. (2017a) investigated the potential of GaoFen-3 for interferometry by generating a digital elevation model (DEM) using two images with a spatial baseline of approximately 600 m and a temporal separation of 116 days. Wang et al. (2019) utilized a small stack of interferograms to map land subsidence in Beijing, China using five GaoFen-3 images, and compared their result with an additional deformation measurement acquired from Sentinel-1B images, demonstrating the prospect of applying GaoFen-3 in land subsidence monitoring. However, few studies have yet been carried out to fully demonstrate the performance of applying GaoFen-3 for monitoring co-seismic deformation.

The interferometric SAR (InSAR) technique, which utilizes phase information, has proven to be capable of mapping topography (Graham 1974) and monitoring land surface deformation. The differential InSAR (DInSAR) technique advances interpretations by eliminating the topographic phase and effectively detecting land surface displacement with high precision (Massonnet et al. 1993). To date, SAR data from various missions have been used extensively for measuring co-seismic deformation and deriving source parameters of a number of earthquakes, e.g. the 1999 Izmit, Turkey, earthquake (Wright 2002); 1999 Duzce, Turkey, earthquake (Burgmann et al. 2002); 2002 moment magnitude ( $M_w$ ) 6.7 Nenana Mountain, Alaska, earthquake (Wright, Lu, and Wicks 2003); 2002  $M_w$  7.9 Denali Fault earthquake (Biggs et al. 2010); 2008  $M$  7.9 Wenchuan earthquake (Tong, Sandwell, and Fialko 2010); 2009  $M_w$  6.3 L'Aquila earthquake (Lanari et al. 2010); 2010  $M_w$  6.8 Yushu, China, earthquake (Li et al. 2011); 2010 Darfield, New Zealand, earthquake (Hu et al. 2012; Beavan et al. 2012); 2014  $M_w$  6.0 Napa, USA, earthquake (Albano et al. 2015); 2015  $M_w$  7.8 Gorkha, Nepal, earthquake and its aftershocks (Feng et al. 2015); and 2016 Central Italy earthquake sequence (Cheloni et al. 2017).

This study presents the first attempt to evaluate the interferometric performance of GaoFen-3 in monitoring co-seismic deformation using the DInSAR technique. First, the interferogram is constructed using GaoFen-3 images that span the 2017 surface-wave magnitude ( $M_s$ ) 7.0 Jiuzhaigou earthquake. Then, by mitigating the severe orbital error phase and unwrapping the deformation field, the co-seismic deformation field is generated. Finally, the fault parameters and slip distribution are inverted from the deformation phase. The interferogram, co-seismic deformation field, fault parameters and slip distribution derived from the GaoFen-3 deformation measurement are compared with those obtained from Radarsat-2, Sentinel-1A and Advanced Land Observing Satellite-2 (ALOS-2) Phased Array type L-band Synthetic Aperture Radar-2 (PALSAR-2). The interferogram and deformation field directly indicate the effectiveness of GaoFen-3 in co-seismic deformation measurements, and the identical fault parameters derived from the GaoFen-3 data indirectly supports the hypothesis that GaoFen-3 is qualified for co-

seismic modelling tasks. The comparison validates GaoFen-3's ability to monitor co-seismic deformation.

## 2. Study area and dataset

The study area is located in Jiuzhaigou County, Sichuan, China, a mountainous region with an average elevation of  $> 4$  km. A  $M_s$  7.0 magnitude earthquake struck this area on 8 August 2017 and the epicentre was located at  $33^{\circ}13'N$  and  $103^{\circ}53'E$ , with a focal depth of 20 km. The earthquake occurred in the northern section of the eastern border of the Bayanhar block. Preliminary teleseismic waveform analysis suggested that the rupture for this event occurred on a buried left-lateral strike-slip fault. It is difficult to acquire and investigate co-seismic deformation due to the dense vegetation coverage, steep terrain, and sparse distribution of global positioning system (GPS) stations. Nie et al. (2018) investigated the fault model of the earthquake estimated from co-seismic deformation observed from GPS and Sentinel-1A data. Zhao et al. (2018) presented deformation field maps from Sentinel-1A and used a one-segment model for inversion and slip distribution analysis. Sun et al. (2018) adopted a joint inversion of the InSAR and teleseismic body wave data and obtained a slip model that is dominated by left-lateral strike-slip motion on a subvertical fault presenting a significant shallow slip deficit. Xie et al. (2018) performed a preliminary analysis on the source and seismogenic structure of the earthquake and indicated that the focal mechanism of the Jiuzhaigou earthquake implied a left-lateral strike-slip fault. Zhang et al. (2018b) inferred that the earthquake involved predominantly left-lateral motion on a north-northwest to south-southwest fault dipping about  $50^{\circ}$  to the southwest based on InSAR (using Sentinel-1A) and GPS measurements, and they also inferred a compact co-seismic slip distribution located in the range of approximately 1–10 km depth below the surface. Liu et al. (2019) analysed GPS and InSAR static displacements, and high-rate GPS and teleseismic dynamic motions of the earthquake, showing a complex slip pattern characterized by two patches with a mean slip of 0.6 m.

The GaoFen-3 dataset, used in this study to capture earthquake movement, consists of two acquisitions in fine strip I mode. Each acquisition contains two frames covering the earthquake area. For comparison, we also obtained two Radarsat-2 images in extra fine mode, four Sentinel-1A (two ascending and two descending) images in interferometric wide (IW) mode and two ALOS-2 PALSAR-2 images in stripmap mode spanning the earthquake event. The scopes of the SAR images are shown in Figure 1 and their parameters are given in Table 1.

## 3. Data processing and inversion method

### 3.1. Data processing

The DInSAR interferograms in this study, including the GaoFen-3 interferogram, are generated by using the Gamma package (Werner et al. 2000). The earthquake area is covered by two consecutive frames of GaoFen-3 in the same path, so the single look complex (SLC) image mosaic is applied first. Then, the signal-to-noise ratio is improved by averaging the GaoFen-3 images with 10 range looks and 10 azimuth looks, equal to pixel

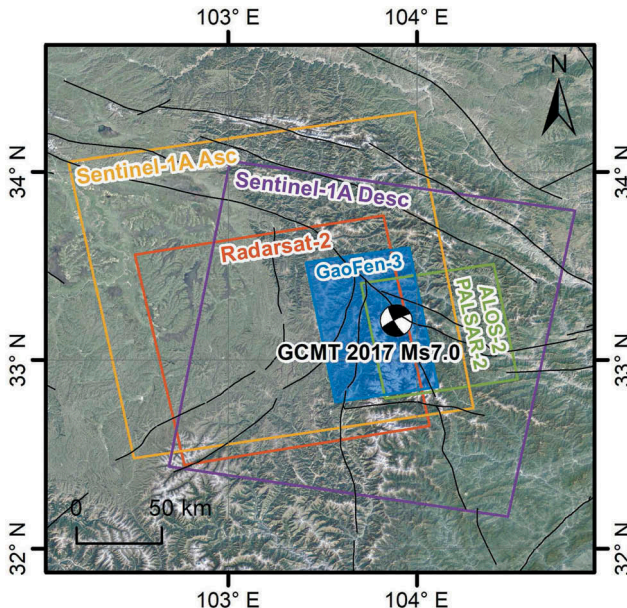


**Figure 1.** The outlines of the SAR images, mapped faults (black lines), the epicentre of the earthquake, and optical images. Beach ball denotes the global centroid moment tensors (GCMT) solution.

**Table 1.** Parameters of SAR images used in this study.

SAR sensors	GaoFen-3	Radarsat-2	Sentinel-1A	Sentinel-1A	ALOS-2 PALSAR-2
Track			128	62	
Inclination	Ascending	Ascending	Ascending	Descending	Ascending
Master date	20170806	20170530	20170730	20170806	20170625
Slave date	20170904	20170810	20170811	20170818	20171029
$\Delta T$ (day)	29	72	12	12	126
$B_{\perp}$ (m)	-254.7	44.6	36.3	-63.6	122.7
Orbital altitude (km)	755	798	693	693	628
Band	C	C	C	C	L
Incidence (°)	42.5	35	39.2	39.2	40.6
Heading (°)	-13.2	-10.8	-12.9	-167.1	-9.9
Pixel spacing (m)	2.25 × 2.86	2.66 × 2.48	2.33 × 13.98	2.33 × 13.98	4.29 × 3.25
Imaging width (km)	50	125	250	250	70
Mode	Fine strip I	Extra fine	IW	IW	Stripmap

IW = Interferometric wide

spacings of 22.48 m and 28.62 m in the range and azimuth directions, respectively. By multiplication of the multi-looked master SLC and the complex conjugate of the registered slave, the interferogram is constructed directly.

To highlight the deformation fringes, we first remove the effect of the reference phase using the initial baseline calculated from the orbital information, and topography phase using the initial baseline and a 1-arc-second Shuttle Radar Topography Mission (SRTM) DEM (Farr et al. 2007; Massonnet and Feigl 1998). We observe dense approximately parallel fringes, which are mainly attributed to orbital errors and possibly attributed to ionospheric anomalies. To further mitigate the orbital error, the reference phase is then calculated and subtracted again through the refined baseline by performing a non-linear

**Table 2.** Baseline of GaoFen-3 interferogram.

	$B_c$ (m)	$B_n$ (m)	$B_c^{\text{rate}}$ (m s $^{-1}$ )	$B_n^{\text{rate}}$ (m s $^{-1}$ )
Initial baseline	-357.575	-41.233	0.0698	0.6217
Precise baseline	-354.097	-46.058	0.8915	-0.5409
Baseline error	3.478	-4.825	0.8217	-1.1626

The subscript  $n$  represents the normal basis vector pointing from the spacecraft to the earth centre, and the subscript  $c$  represents the cross-track basis vector which is formed from the cross-product of the normal basis vector and the spacecraft velocity state vector (Small, Werner, and Nuesch 1993).  $B$  represents the baseline,  $B_c$  and  $B_n$  represent the components of mid-scene baseline in the directions of  $c$  and  $n$ , and  $B_c^{\text{rate}}$  and  $B_n^{\text{rate}}$  represent the components of the baseline change rates in the directions of  $c$  and  $n$ .

least square (LS) fit, which uses the iterative Levenberg-Marquardt algorithm based on the ground control points (Small, Werner, and Nuesch 1993).

The initial baseline, the refined baseline and their difference, which indicates the mitigated baseline error from the LS method, are shown in Table 2. Subsequent to the mitigation of the orbital error phase, however, some residual quadratic phase ramps still remain in the interferogram, which is mainly caused by the misestimation of orbital error due to the influence of the deformation phase. Consequently, the residual effects of topography are removed with the refined baseline. Containing the residual orbital error phase, the interferogram is filtered with the adaptive filtering method (Goldstein and Werner 1998) through an exponent for non-linear filtering  $\alpha$  of 0.8 and a filtering fast Fourier transformation window size of 16. The highly coherent area whose coherence is greater than 0.4 is unwrapped with the minimum cost flow algorithm (Werner et al. 2000). Finally, the residual phase fringes are fitted to a quadratic surface by the far-field phase using a quadratic model (Hanssen 2001) and removed, assuming that the far-field displacement is negligible (Massonnet et al. 1993) and that the fringes are caused by orbital error only.

Figure 2 shows the two-step procedure for orbital error mitigation. After eliminating the orbital error phase (Figure 2(b)) by using the LS method from the initial interferogram phase (Figure 2(a)), and removing the quadratic phase (Figure 2(d)) from the interferometric phase

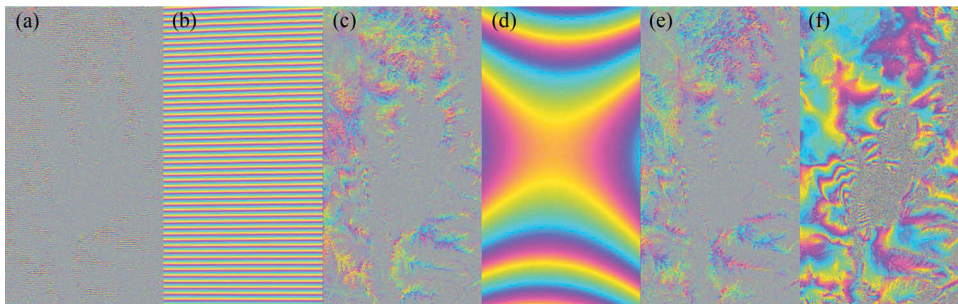


**Figure 2.** Interferometric phase during the orbital error mitigation process. (a) GaoFen-3 interferometric phase with initial baseline. (b) Simulated phase caused by baseline error calculated with the LS method. (c) Interferometric phase with refined baseline by the LS method. (d) Quadratic phase fitted from the unwrapped phase. (e) Interferometric phase with baseline re-refined by a quadratic model. (f) Filtered interferometric phase. All images are in SAR coordinates. Each colour cycle represents an area of phase ranging from 0 to  $2\pi$ .

(Figure 2(c)) with refined baseline by the LS method, there eventually remain no obvious global fringes in the interferogram (Figure 2(e)), implying that the orbital error phase is removed and that the remaining phases are thus mainly the deformation phase and the atmospheric phase.

To increase phase coherence and reduce the phase noise in the interferogram, a multi-look approach (Scheiber and Bothale 2002) (i.e. 3 looks in the range direction combined with 3 looks in the azimuth direction) is adopted. Thus, the interferometric image is multi-looked into a pixel size of about 80 m. To visualize the co-seismic fringes, the phase is wrapped again and filtered twice using the adaptive filtering method with an  $\alpha$  of 0.8 and filtering fast Fourier transformation window sizes of 16 and 32. The filtered interferometric phase is shown in Figure 2(f). The interferogram and the deformation field in the line of sight (LOS) direction are geocoded to the World Geodetic System (WGS) 84 coordinates.

Regarding the data processing procedures for the other sensors, Radarsat-2 and ALOS-2 PALSAR-2 have fewer orbital errors, which are easily corrected. The processing of these two is almost the same as that of GaoFen-3. Sentinel-1A carries a C-band microwave sensor running in terrain observation with progressive scans (TOPS) mode with precise orbits provided by the European Space Agency. To compensate for the residual azimuth phase ramp due to possible misregistration in the azimuth direction, the enhanced spectral diversity method (Prats-Iraola et al. 2012) is applied in overlapping areas across adjacent bursts. This procedure is in addition to the data processing of GaoFen-3.

### 3.2. Fault modelling and slip distribution inversion

For the purpose of further investigating GaoFen-3's applicability to co-seismic deformation, fault modelling and slip distribution are applied, and the results are compared across multiple data sources, including organizations and previous studies. Focal mechanism solutions for the Jiuzhaigou earthquake from different organizations are listed in Table 3. The strike, dip and slip angles vary from  $151^\circ$  to  $153^\circ$ ,  $75^\circ$  to  $84^\circ$ , and  $-8^\circ$  to  $-33^\circ$ , respectively, which indicates that the co-seismic rupture was caused by left-lateral strike-slip movement. These values are consequently used as the initial input model parameters for the following fault modelling and slip inversion. We also list the source mechanism parameters derived from other studies in Table 4. Based on the above parameters and previous studies, we assume two possible dislocation models, which are a simple uniform slip model and a more complex distributed model.

**Table 3.** Focal mechanism solution for the Jiuzhaigou event.

Source	$M_w$	Lon. (E)	Lat. (N)	Depth (km)	Fault plane 1			Fault plane 2		
					Strike (°)	Dip (°)	Rake (°)	Strike (°)	Dip (°)	Rake (°)
GCMT	6.5	103°53'	33°13'	16.2	243	82	-168	151	79	-8
USGS	6.5	103°51'	33°12'	13.5	246	57	-173	153	84	-33
IPGP	6.6	103°51'	33°13'	8	244	81	-165	151	75	-9
CEAIGP	6.5	103°49'	33°12'	11	64	77	-151	326	62	-15

GCMT = Global Centroid Moment Tensors; USGS = United States Geological Survey; IPGP = Institut de Physique du Globe de Paris; CEAIGP = Institute of Geophysics, China Earthquake Administration. Lon. = longitude. Lat. = latitude.

**Table 4.** The source mechanism parameters previously derived from geodetic observations.

$M_w$	Focal mechanism			Focal distribution				Source
	Strike (°)	Dip (°)	Rake (°)	Length (km)	Width (km)	Slip (m)	Depth	
6.46	–	90 <sup>&lt;</sup> 16km	341	26 <sup>SE</sup>	26	~0.77 <sup>M</sup>	9 <sup>MS</sup>	Ji et al. 2017 <sup>InSAR</sup>
	–	61 <sup>&gt;</sup> 16km						
	–	90 <sup>&lt;</sup> 16km	329	20 <sup>NW</sup>	26			
	–	75 <sup>&gt;</sup> 16km						
6.36	150	80	–20	–	–	–	~22	Yang et al. 2017
	244	70	–169	–	–	–	–	
6.5	~150	~80	~–19.5 <sup>A</sup>	32	20	~1 M	~11	Zhang et al. 2017b <sup>InSAR</sup>
6.5	153	50	–9 <sup>A</sup>	40	30	~1	~8 <sup>MS</sup>	Shan et al. 2015 <sup>InSAR</sup>
6.4	326	60	–15 <sup>A</sup>	80	40	0.4 <sup>M</sup>	–	Wang et al. 2018b
6.5	152	74	8	–	–	–	–	Xie et al. 2018
6.5	153	84	–33	–	–	~1.4 <sup>M</sup>	5–15	Li et al. 2018
6.5	155	80	–10 <sup>A</sup>	35	25	~1.3 <sup>M</sup>	~6 <sup>MS</sup>	Zhao et al. 2018 <sup>InSAR</sup>
6.49	155	81	–11	40	30	0.85 <sup>M</sup>	~11 <sup>MS</sup>	Nie et al. 2018 <sup>InSAR</sup>
6.57	–	–	–	40	32	0.73 <sup>M</sup>	~10 <sup>MS</sup>	Shen, Luo, and Jiao 2018
6.5	153	50	–12	–	–	~1 M	6 <sup>MS</sup>	Zhang et al. 2018b
6.54	~154	~77	~7.84	23	11	~1.06 <sup>M</sup>	5–9 <sup>MS</sup>	Hong et al. 2018 <sup>InSAR</sup>
–	~150 <sup>S</sup>	~75	–	–	–	–	7.3 <sup>A</sup>	Long et al. 2019
	~159 <sup>N</sup>	~59	–	–	–	–	–	
6.5	153	70	–	42	27	~1.5 <sup>M</sup>	–	Liu, Yin, and Wang 2019
6.6	–	88	–	30	20	0.6 <sup>A</sup>	–	Liu et al. 2019 <sup>InSAR</sup>

The superscript SE represents south-east, the superscript NW represents north-west, the superscript S represents the south, the superscript N represents north, the superscript A represents the average value, the superscript M represents the maximum, and the superscript MS represents the maximal slip. The superscript InSAR means that the study are with the inversion of the InSAR data. ~ means approximately.

### 3.2.1. Uniform slip model

A single rectangular uniform slip in an elastic half-space was initially modelled (Okada 1985). We used a freely available MATLAB-based geodetic Bayesian inversion software (GBIS) package (Marco and Hooper 2018), which presents a Bayesian approach that allows characterization of posterior probability density functions of source model parameters. To prepare the data for inversion, the points with coherence coefficients above 0.4 were retained as high-quality points. Adaptive quadtree sampling was employed to downsample data points in order to make the computation feasible and efficient. The quadtree threshold variance was set to 0.0052 to obtain a higher density of sampling points in the near-field region. For Radarsat-2, Sentinel-1A ascending and Sentinel-1A descending data, the quadtree threshold variances were set to 0.0052, 0.0052 and 0.0042, respectively. The final numbers of data points were 1743 for GaoFen-3, 983 for Radarsat-2, 964 for Sentinel-1A ascending and 1017 for Sentinel-1A descending, with few spatial characteristics of the co-seismic deformation lost in this process. Then, we chose a kinematic forward model for a rectangular dislocation source with 9 source model parameters: length, width, depth of the lower edge, dip angle, strike angle, x and y coordinates of the midpoint of the lower edge, uniform slip in the strike direction, and uniform slip in the dip direction. Since all InSAR measurements were relative to an independent reference point, the GBIS provided the choice to estimate the rigid shift in the LOS direction and the coefficients for a linear ramp for each interferogram. Priors for fault geometry were based on previous results from Tables 3 and 4. Finally, the optimal fault parameters (i.e. length, width, depth, dip, strike, longitude, latitude) were determined by the GBIS software.

### 3.2.2. *Distributed slip model*

A distributed slip model was also conducted according to the study by Zhao et al. (2018). The slip distribution inversion was conducted using a one-segment fault slip model based on a homogeneous elastic half-space model (Okada 1985) assuming Poisson ratios of 0.25. An inversion code, steepest descent method (SDM), developed by Wang, Diao, and Hoechner (2013) was used to invert for the co-seismic slip distribution on the fault. There were 9 inputs needed for this programme, including the latitude ( $33^{\circ}23'N$ ) and longitude ( $103^{\circ}45'E$ ) of the reference point, the length (35 km) and the width of the rectangular fault (25 km), the length (1 km) and width (1 km) of the subdivided rectangular patches, the dip angle ( $80^{\circ}$ ), the strike angle ( $155^{\circ}$ ), and the rake angle (ranging from  $-45^{\circ}$  to  $45^{\circ}$ ) of the fault, and the maximum slip depth (15 m). All the parameters were set according to the work of Zhao et al. (2018).

## 4. Results and comparisons

As there is no previous study on the application of GaoFen-3 to monitoring co-seismic deformation to evaluate the potential of GaoFen-3 in this field, the deformation results are compared with Radarsat-2 ascending, Sentinel-1A ascending and descending, and ALOS-2 PALSAR-2 ascending results. To achieve this comparison, three indicators are adopted in our research: the interferogram and its coherence, the deformation field, and the derived fault parameters and slip distribution. The interferogram and its coherence can be applied to estimate the interferometric quality. The deformation field can evaluate the accuracy of the InSAR measurement directly. The derived fault parameters and slip distribution can indirectly discriminate the InSAR modelling capability. In this section, we analyse in more detail the similarity and differences between interferograms and their statistical coherences, deformation fields, and inverted fault parameters and slip distributions from different sensors.

### 4.1. *Interferograms and coherence*

The GaoFen-3 interferogram with WGS 84 coordinates is depicted in Figure 3(a). Good coherence results are shown in most of the study areas, especially in the northwest part of the epicentre zone, which makes the phase convincing. The whole displacement field covers an area of approximately  $50 \times 50$  km. Five cycles are measured, with each cycle representing 28 mm displacement in the LOS direction. The deformation field shows positive and negative values and is asymmetric on both sides of the source fault with a NW strike, which implies left-lateral strike-slip motion. The deformation in the intermediate field can hardly be measured due to the decorrelation caused by a number of factors including intense ground deformation and large displacement gradients.

The other four interferograms (Figure 3(b–e)) derived from Radarsat-2, Sentinel-1A ascending and descending, and ALOS-2 PALSAR-2 depict all the co-seismic deformation, some post-seismic deformation and some atmospheric phases. These interferometric fringes are relatively clear and continuous, except in the near-field of the seismogenic fault. Apparently, the overall patterns of all five co-seismic deformation fields are consistent. The clear fringes also demonstrate that the fault experienced left-lateral strike-slip motion. The GaoFen-3, Radarsat-2 and Sentinel-1A ascending interferograms show similar

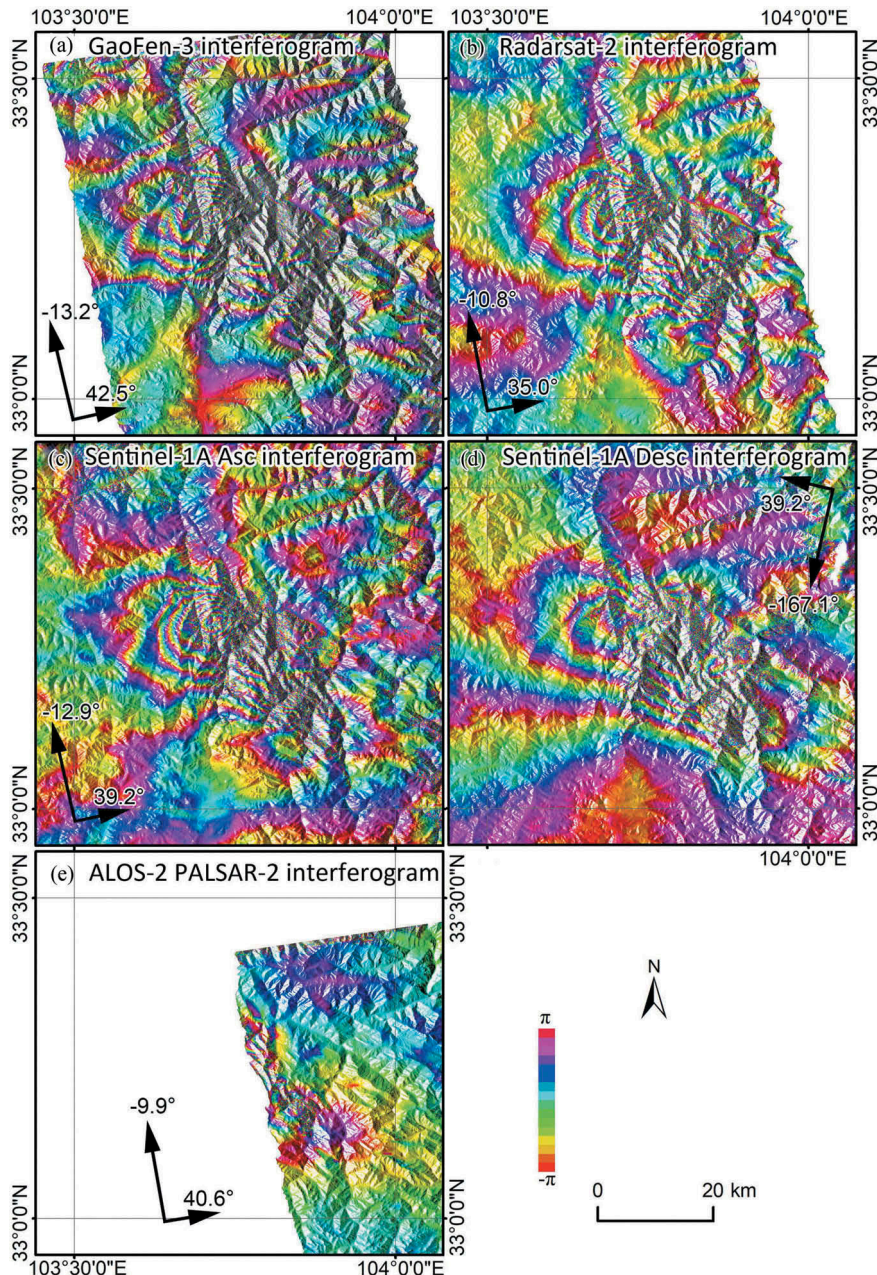


**Figure 3.** Interferograms from GaoFen-3 (a), Radarsat-2 (b), Sentinel-1A (c, d) and ALOS-2 PALSAR-2 (e). Temporal and spatial perpendicular baselines are 29 days and  $-254.7\text{ m}$  for GaoFen-3, 72 days and  $44.6\text{ m}$  for Radarsat-2, 12 days and  $36.3\text{ m}$  for Sentinel-1A ascending, 12 days and  $-63.6\text{ m}$  for Sentinel-1A descending, and 126 days and  $122.7\text{ m}$  for ALOS-2 PALSAR-2.

fringe patterns since they operate at the same C-band wavelength and have similar viewing geometries. Their slight discrepancies are due to the divergence in heading

and incident angles and different post-seismic deformation and atmospheric delay at different observation times.

The coherences of interferograms are also calculated and compared. All the coherence maps of the overlapping area among GaoFen-3, Radarsat-2, and Sentinel-1A are clipped, and their coherences are counted and illustrated in [Figure 4](#). The mean of GaoFen-3 coherence is 0.206, and the standard deviation is 0.028. Correspondingly, the spatial and temporal baselines of GaoFen-3 are  $-254.7$  m and 29 days, respectively ([Table 1](#)). The mean coherence for Radarsat-2 is 0.118, and the standard deviation is 0.030, and the mean is much lower than that of GaoFen-3. This is because Radarsat-2 uses the same band (C-band) wavelength as the GaoFen-3 sensor and possesses a slightly shorter spatial baseline (44.6 m) but a much longer temporal baseline (72 days) in its interferogram. The Sentinel-1A means (0.317 for ascending and 0.282 for descending) are higher than GaoFen-3 ([Table 1](#)). The deviations of Sentinel-1A ascending and descending are 0.044 and 0.038, respectively. Both ascending and descending Sentinel-1A data have short temporal baselines with a revisit period of 12 days. In addition, their precise orbital information barely makes the orbital error phase in the two interferograms. These two factors lead to better coherence and clear and relatively continuous fringes. ALOS-2 PALSAR-2 has a long-time interval of 126 days and a relatively small spatial baseline of 122.7 m. It operates at the L-band wavelength, preserving better coherence than the C-band in vegetated areas. Even so, all coherences are low as the earthquake occurred in summer and the study area is covered by dense vegetation. The images acquired from ALOS-2 PALSAR-2 are not utilized in the coherence calculation, fault modelling and slip distribution inversion steps because they cover only parts of the earthquake area.

#### 4.2. Co-seismic deformation fields

The deformation fields of Radarsat-2 and Sentinel-1A ascending are compared with that of GaoFen-3 as these three missions have similar viewing geometries. Considering the different incident angles and supposing that displacement occurred in the ground range direction, the ratios of displacement in the LOS direction of the Radarsat-2 and Sentinel-1A deformation fields to that of GaoFen-3 are  $\sin 35^\circ (\sin 42.5^\circ)^{-1} = 0.85$  and  $\sin 39.2^\circ (\sin 42.5^\circ)^{-1} = 0.94$ , respectively. Since both of the ratios are close to 1, the differences between the displacements in LOS directions from the three data sources are relatively small. Therefore, we ignore the errors caused by the differences in incident and heading angle. The images of the Radarsat-2

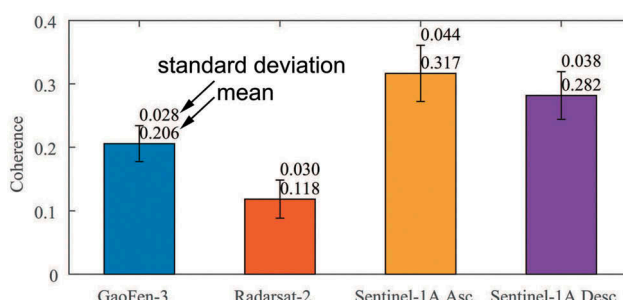


**Figure 4.** Coherence of four interferograms.

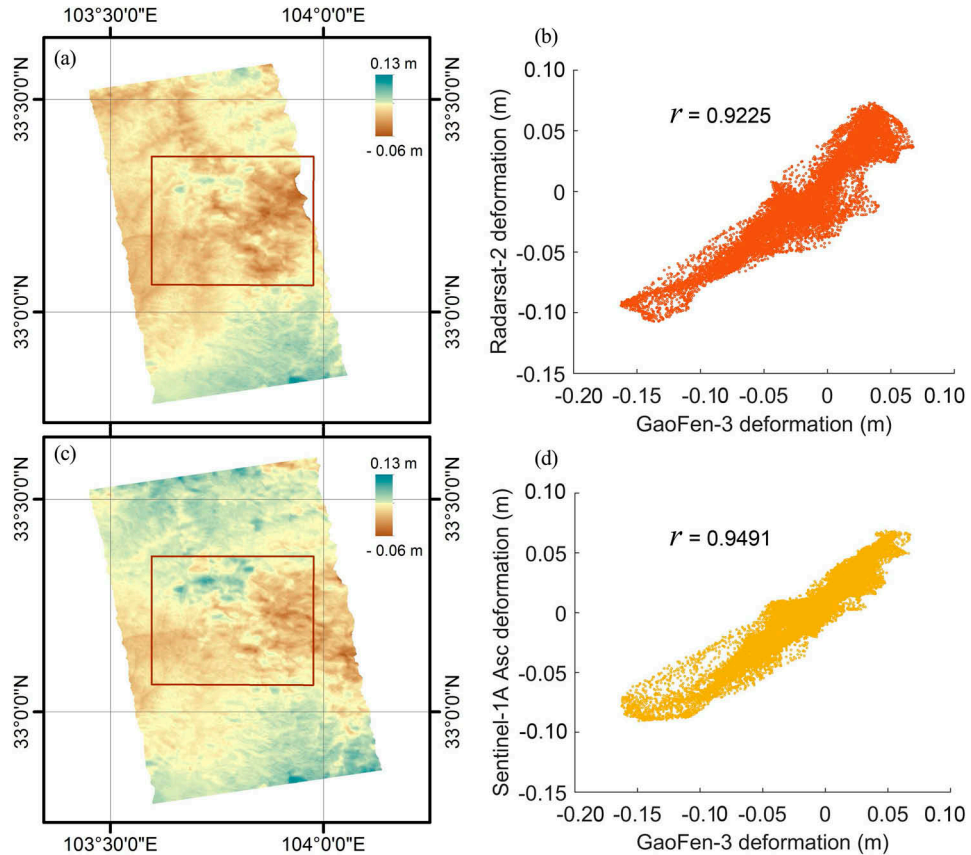


**Figure 5.** Deformation field from GaoFen-3 compared with those from Sentinel-1A ascending and Radarsat-2. (a) Difference between Radarsat-2 and GaoFen-3 deformation fields. (b) Correlation plots between GaoFen-3 and Radarsat-2 deformation fields. (c) Difference between Sentinel-1A ascending and GaoFen-3 deformation fields within the red boundary. (d) Correlation plots between GaoFen-3 and Sentinel-1A ascending deformation fields within the red boundary.

and Sentinel-1A deformation fields are resampled to the same resolution and pixel location as GaoFen-3. We obtain the difference between the deformation fields of Radarsat-2 and GaoFen-3 (Figure 5(a)), which does not exhibit any visible deformation signal. A scatter plot between the LOS deformation fields of Radarsat-2 and GaoFen-3 for each pixel location in the near-field area is illustrated in Figure 5(b), showing a clear linear correlation with the Pearson's correlation coefficient ( $r$ ) reaching 0.9225. The same comparison process is applied to the deformation field of Sentinel-1A ascending. The difference between the deformation fields of Sentinel-1A ascending and GaoFen-3 also shows no obvious deformation information (Figure 5(c)) and the  $r$  reaches 0.9491 (Figure 5(d)). We further note that the differences have biases of approximately 5 cm (Radarsat-2) and 7 cm (Sentinel-1A ascending) around the deformation of  $-15$  cm of GaoFen-3. Most of the differences are attributed to atmospheric noise.

### 4.3. Fault parameters and slip distribution

#### 4.3.1. Uniform slip model

For the uniform slip model, the optimal length, width, and depth of the fault inverted from GaoFen-3 data are 24.47 km, 10.89 km, and 11.96 km, respectively. The dip and strike angles are  $57.48^\circ$  and  $149.86^\circ$ , respectively. The slip direction is consistent with that of a thrust fault with a left-lateral component, with 0.57 m in the strike direction and  $-0.01$  m in the slip direction. The optimal fault parameters inverted from GaoFen-3 are shown in Table 5. The fault parameters from GaoFen-3 data resembled those from Radarsat-2, Sentinel-1A ascending, and previous studies listed in Table 4. However, there is a little discrepancy compared with the fault parameters provided by the institutions listed in Table 3.

The inverted fault parameters were employed to simulate deformation. Figure 6 illustrates the observed LOS displacement Figure 6 (a-d), simulated LOS displacement Figure 6(e-h) predicted by the optimal uniform slip model, and the residuals Figure 6(i-l) between the simulated and observed data sources. The observed and simulated coseismic deformations are well reconciled, and the residual interferograms exhibit random spatially-correlated errors that vary in each independent interferogram. The comparison results indicate that the fault parameters are appropriate for this event, and provide evidence that GaoFen-3 performs as well as Radarsat-2 and Sentinel-1A in fault modelling. However, mismatches between observations and predictions are shown in the near field (Figure 6(i-l)). One probable cause refers to that a simple elastic dislocation generally lacks the capability to model the near-fault process (Funning, Parsons, and Wright 2010).

**Table 5.** Optimal fault parameters derived from four InSAR observations.

Source	Length (km)	Width (km)	Depth (km)	Dip ( $^\circ$ )	Strike ( $^\circ$ )	Lon. (E)	Lat. (N)
GaoFen-3	24.47	10.89	11.96	57.48	149.86	103°45'	33°11'
Radarsat-2	22.57	9.95	12.38	59.17	155.26	103°45'	33°12'
Sentinel-1A Asc	25.13	6.15	10.49	57.52	146.29	103°47'	33°13'
Sentinel-1A Desc	33.58	16.62	19.69	80.84	166.45	103°49'	33°15'

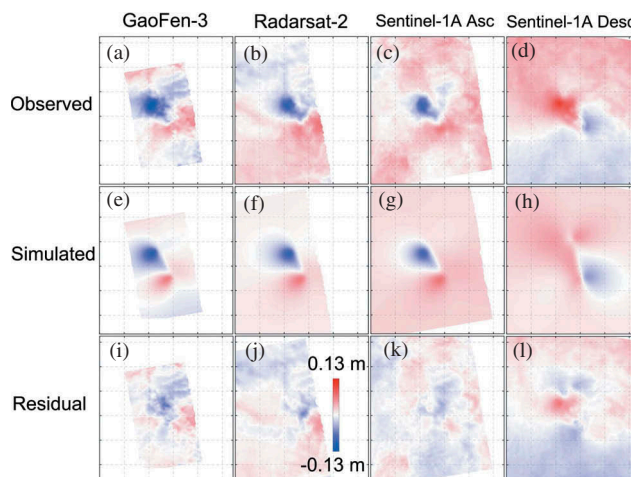


**Figure 6.** Observed (a-d), simulated (e-h) and residual (i-l) LOS displacement maps from GaoFen-3, Radarsat-2, and Sentinel-1A ascending and descending.

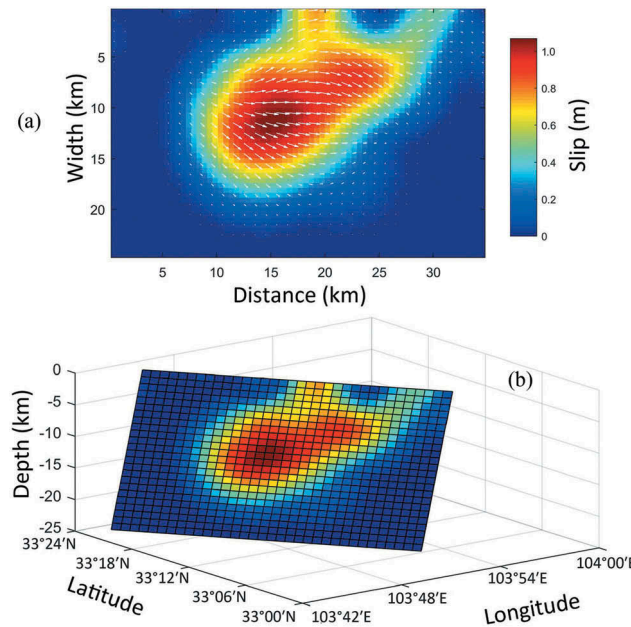


**Figure 7.** Fault slip distribution in two (a) and three (b) dimensional views inferred from GaoFen-3 deformation data. Colours show the magnitude of slip; arrows show relative motion.

#### 4.4. Distributed slip model

The fault slip distribution inferred from GaoFen-3 observations is illustrated in Figure 7. The resultant slip model shows a simple, elliptical pattern of slip, reaching a maximum of approximately 1 m at depths of 10–13 km. The rake angle is almost  $0^\circ$ , which suggests left-lateral strike-slip motion for this fault. Similarly, in the study of Zhao et al. (2018), the slip distribution constrained by ascending InSAR data presented a concentrated high-slip patch with a magnitude of  $> 0.4$  m at depths of 5–15 km; a peak slip of 0.9 m occurred at a depth of about 10 km. This result also shows that GaoFen-3 has almost the same capability as Sentinel-1A in slip inversion for an earthquake.

To summarize, the interferograms, co-seismic deformation field, fault parameters and slip distribution obtained from GaoFen-3 are compared with those acquired from Radarsat-2 and Sentinel-1A in this section. Both the direct comparison of interferograms and co-seismic deformation field and the indirect comparison of fault parameters and slip distributions suggest that GaoFen-3 has the capability to monitor co-seismic deformation with almost the same quality level as the prevalent SAR sensors in the 2017  $M_s$  7.0 Jiuzhaigou earthquake.

## 5. Conclusion

This paper reports the first effort to explore the interferometric capability of GaoFen-3 in monitoring co-seismic deformation, fault modelling, and slip distribution reversion. The interferogram, deformation field, fault parameters and slip distribution obtained from GaoFen-3 are compared to those acquired from Radarsat-2, Sentinel-1A, and ALOS-2 PALSAR-2. The analysis of the comparison results shows that (1) the interferogram from

GaoFen-3 presents visible co-seismic fringes and has patterns similar to those obtained from Radarsat-2 and Sentinel-1A ascending; (2) the near-field co-seismic deformation acquired from GaoFen-3 shows evident linear correlations with Radarsat-2 and Sentinel-1A ascending, and the  $r$  values reach 0.9225 and 0.9491, respectively; and (3) the derived fault parameters and slip distribution from GaoFen-3 are very close to those derived from Radarsat-2 and Sentinel-1A ascending. All comparisons demonstrate that GaoFen-3 performs well in co-seismic deformation monitoring, fault modelling and slip distribution inversion. Therefore, GaoFen-3 can be a powerful tool for measuring co-seismic deformation. For future work, if the GaoFen-3 orbit accuracy cannot be improved, orbital error mitigation processing should be considered during GaoFen-3 interferometry.

## Acknowledgements

We would like to thank the National Satellite Ocean Application Service for providing GaoFen-3 data, the Canadian Space Agency (CSA) for providing RADARSAT-2 data, the European Space Agency (ESA) for providing Sentinel-1A data and the Japan Aerospace Exploration Agency (JAXA) for providing ALOS-2 PALSAR-2 data. We gratefully acknowledge the anonymous reviewers for giving constructive comments and suggestions to help improve earlier version of the manuscript.

## Disclosure Statement

No potential conflict of interest was reported by the authors.

## Funding

This work was supported by the National Natural Science Foundation of China [Grant Number 61427802, 41374016, 41330634].

## References

Albano, M., M. Polcari, C. Bignami, E. Trasatti, M. Moro, S. Stramondo, and U. Wegmuller. 2015. "Sentinel-1 InSAR: First Results from Seismic and Volcanic Applications." In *EGU General Assembly Conference*, Vienna, Austria Vol. 17.

Beavan, J., M. Motagh, E. J. Fielding, N. Donnelly, and D. Collett. 2012. "Fault Slip Models of the 2010–2011 Canterbury, New Zealand, Earthquakes from Geodetic Data and Observations of Postseismic Ground Deformation." *New Zealand Journal of Geology and Geophysics* 55 (3): 207–221. doi:[10.1080/00288306.2012.697472](https://doi.org/10.1080/00288306.2012.697472).

Biggs, J., R. Burgmann, J. T. Freymueller, Z. Lu, B. Parsons, I. Ryder, G. Schmalzle, and T. Wright. 2010. "The Postseismic Response to the 2002 M 7.9 Denali Fault Earthquake: Constraints from InSAR 2003–2005." *Geophysical Journal of the Royal Astronomical Society* 176 (2): 353–367. doi:[10.1111/j.1365-246X.2008.03932.x](https://doi.org/10.1111/j.1365-246X.2008.03932.x).

Burgmann, R., M. E. Ayhan, E. J. Fielding, T. J. Wright, S. McClusky, B. Aktug, C. Demir, O. Lenk, and A. Turkezer. 2002. "Deformation during the 12 November 1999 Duzce, Turkey, Earthquake, from GPS and InSAR Data." *Bulletin of the Seismological Society of America* 92 (1): 161–171. doi:[10.1785/0120000834](https://doi.org/10.1785/0120000834).

Cheloni, D., V. De Novellis, M. Albano, A. Antonioli, M. Anzidei, S. Atzori, A. Avallone, et al. 2017. "Geodetic Model of the 2016 Central Italy Earthquake Sequence Inferred from InSAR and GPS Data." *Geophysical Research Letters* 44 (13): 6778–6787. DOI:[10.1002/2017GL073580](https://doi.org/10.1002/2017GL073580).

Chen, Q., T. Li, X. Tang, X. Gao, and X. Zhang. 2018. "Preliminary GaoFen-3 InSAR DEM Accuracy Analysis." *ISPRS - International Archives of the Photogrammetry, Remote Sensing and Spatial Information Sciences* XLII-3: 173–177. doi:[10.5194/isprs-archives-XLII-3-173-2018](https://doi.org/10.5194/isprs-archives-XLII-3-173-2018).

Fan, Z., X. Yao, H. Tang, Y. Qiang, Y. Hu, and B. Lei. 2018. "Multiple Mode SAR Raw Data Simulation and Parallel Acceleration for GaoFen-3 Mission." *IEEE Journal of Selected Topics in Applied Earth Observations and Remote Sensing* PP 99: 1–12.

Fang, Y., H. Zhang, Q. Mao, and Z. Li. 2018. "Land Cover Classification with GF-3 Polarimetric Synthetic Aperture Radar Data by Random Forest Classifier and Fast Super-Pixel Segmentation." *Sensors* 18 (7): 2014. doi:[10.3390/s18072014](https://doi.org/10.3390/s18072014).

Farr, T. G., P. A. Rosen, E. Caro, R. Crippen, R. Duren, S. Hensley, M. Kobrick, M. Paller, E. Rodriguez, and L. Roth. 2007. "The Shuttle Radar Topography Mission." *Reviews of Geophysics* 45 (2): 361. doi:[10.1029/2005RG000183](https://doi.org/10.1029/2005RG000183).

Feng, G., Z. Li, X. Shan, L. Zhang, G. Zhang, and J. Zhu. 2015. "Geodetic Model of the 2015 April 25 M W 7.8 Gorkha Nepal Earthquake and M W 7.3 Aftershock Estimated from InSAR and GPS Data." *Geophysical Journal International* 203 (2): 896–900. doi:[10.1093/gji/ggv335](https://doi.org/10.1093/gji/ggv335).

Funning, G. J., B. Parsons, and T. J. Wright. 2010. "Fault Slip in the 1997 Manyi, Tibet Earthquake from Linear Elastic Modelling of InSAR Displacements." *Geophysical Journal of the Royal Astronomical Society* 169 (3): 988–1008. doi:[10.1111/j.1365-246X.2006.03318.x](https://doi.org/10.1111/j.1365-246X.2006.03318.x).

Goldstein, R. M., and C. L. Werner. 1998. "Radar Interferogram Filtering for Geophysical Applications." *Geophysical Research Letters* 25 (21): 4035–4038. doi:[10.1029/1998GL900033](https://doi.org/10.1029/1998GL900033).

Graham, L. C. 1974. "Synthetic Interferometer Radar for Topographic Mapping." *Proceedings of the IEEE* 62 (6): 763–768. doi:[10.1109/PROC.1974.9516](https://doi.org/10.1109/PROC.1974.9516).

Hanssen, R. F. 2001. *Radar Interferometry: Data Interpretation and Error Analysis*. Vol. 2. Kluwer Academic Publishers.

Hao, S., Q. Zhang, M. Bian, H. Wang, Z. Wang, L. Chen, and J. Yang. 2018. "A Novel Ship Detection Method Based on Gradient and Integral Feature for Single-Polarization Synthetic Aperture Radar Imagery." *Sensors* 18 (2): 563. doi:[10.3390/s18020563](https://doi.org/10.3390/s18020563).

Hong, S., X. Zhou, K. Zhang, G. Meng, Y. Dong, X. Su, L. Zhang, S. Li, and K. Ding. 2018. "Source Model and Stress Disturbance of the 2017 Jiuzhaigou Mw 6.5 Earthquake Constrained by InSAR and GPS Measurements." *Remote Sensing* 10 (9): 1400. doi:[10.3390/rs10091400](https://doi.org/10.3390/rs10091400).

Hu, J., Z. Li, X. Ding, J. Zhu, L. Zhang, and Q. Sun. 2012. "3D Coseismic Displacement of 2010 Darfield, New Zealand Earthquake Estimated from Multi-Aperture InSAR and D-InSAR Measurements." *Journal of Geodesy* 86 (11): 1029–1041. doi:[10.1007/s00190-012-0563-6](https://doi.org/10.1007/s00190-012-0563-6).

Ji, L., C. Liu, J. Xu, L. Liu, F. Long, and Z. Zhang. 2017. "InSAR Observation and Inversion of the Seismogenic Fault for the 2017 Jiuzhaigou M(s) 7. 0 Earthquake in China." *Chinese Journal of Geophysics (In Chinese)* 60 (10): 4069–4082.

Kang, W., Y. Xiang, F. Wang, L. Wan, and H. You. 2018. "Flood Detection in GaoFen-3 SAR Images via Fully Convolutional Networks." *Sensors* 18 (9): 2915. doi:[10.3390/s18092915](https://doi.org/10.3390/s18092915).

Lanari, R., P. Berardino, M. Bonano, F. Casu, A. Manconi, M. Manunta, M. Manzo, A. Pepe, S. Pepe, and E. Sansosti. 2010. "Surface Displacements Associated with the L'Aquila 2009 Mw 6.3 Earthquake (Central Italy): New Evidence from SBAS-DInSAR Time Series Analysis." *Geophysical Research Letters* 37 (20). doi:[10.1029/2010GL044780](https://doi.org/10.1029/2010GL044780).

Lei, W., B. Han, X. Yuan, B. Lei, C. Ding, Y. Yao, and Q. Chen. 2018. "A Preliminary Analysis of Wind Retrieval, Based on GF-3 Wave Mode Data." *Sensors* 18 (5): 1604. doi:[10.3390/s18051604](https://doi.org/10.3390/s18051604).

Li, Q., K. Tan, D. Wang, B. Zhao, R. Zhang, Y. Li, and Y. Qi. 2018. "Joint Inversion of GNSS and Teleseismic Data for the Rupture Process of the 2017 Mw 6.5 Jiuzhaigou, China, Earthquake." *Journal of Seismology* 22 (3): 805–814. doi:[10.1007/s10950-018-9733-1](https://doi.org/10.1007/s10950-018-9733-1).

Li, Z., J. R. Elliott, W. Feng, J. A. Jackson, B. E. Parsons, and R. J. Walters. 2011. "The 2010 Mw 6.8 Yushu (Qinghai, China) Earthquake: Constraints Provided by InSAR and Body Wave Seismology." *Journal of Geophysical Research Solid Earth* 116: B10302.

Liu, G., W. Xiong, Q. Wang, X. Qiao, K. Ding, X. Li, and S. Yang. 2019. "Source Characteristics of the 2017 Ms 7.0 Jiuzhaigou, China, Earthquake and Implications for Recent Seismicity in Eastern Tibet." *Journal of Geophysical Research: Solid Earth* 124 (5): 4895–4915.

Liu, J., X. Qiu, and H. Wen. 2016. "Automated Ortho-rectified SAR Image of GF-3 Satellite Using Reverse-Range-Doppler Method." In *Geoscience and Remote Sensing Symposium, Beijing, China* 4445–4448. IEEE.

Liu, Q., D. Yin, and Z. Wang. 2019. "Inversion of the Rupture Process and High-frequency Radiation of the 2017 Jiuzhaigou Earthquake, Northeastern Tibetan Plateau." *Journal of Asian Earth Sciences* 179: 300–318. doi:[10.1016/j.jseaes.2019.04.016](https://doi.org/10.1016/j.jseaes.2019.04.016).

Long, F., G. Yi, S. Wang, Y. Qi, and M. Zhao. 2019. "Geometry and Tectonic Deformation of the Seismogenic Structure for the 8 August 2017 Ms 7.0 Jiuzhaigou Earthquake Sequence, Northern Sichuan, China." *Earth and Planetary Physics* 3 (3): 253–267. doi:[10.26464/epp2019027](https://doi.org/10.26464/epp2019027).

Marco, B., and A. Hooper. 2018. "Inversion of Surface Deformation Data for Rapid Estimates of Source Parameters and Uncertainties: A Bayesian Approach." *Geochemistry, Geophysics, Geosystems* 19 (7): 2194–2211. doi:[10.1029/2018GC007585](https://doi.org/10.1029/2018GC007585).

Massonnet, D., and K. L. Feigl. 1998. "Radar Interferometry and Its Application to Changes in the Earth's Surface." *Reviews of Geophysics* 36 (4): 441–500. doi:[10.1029/97RG03139](https://doi.org/10.1029/97RG03139).

Massonnet, D., M. Rossi, C. Carmona, F. Adragna, G. Peltzer, K. Feigl, and T. Rabaute. 1993. "The Displacement Field of the Landers Earthquake Mapped by Radar Interferometry." *Nature* 364 (6433): 138–142. doi:[10.1038/364138a0](https://doi.org/10.1038/364138a0).

Meng, A., Q. Sun, J. Hu, Y. Tang, and Z. Zhu. 2018. "Coastline Detection with Gaofen-3 SAR Images Using an Improved FCM Method." *Sensors* 18 (6): 431.

Nie, Z., D. Wang, Z. Jia, P. Yu, and L. Li. 2018. "Fault Model of the 2017 Jiuzhaigou Mw 6.5 Earthquake Estimated from Coseismic Deformation Observed Using Global Positioning System and Interferometric Synthetic Aperture Radar Data." *Earth Planets and Space* 70 (1): 55. doi:[10.1186/s40623-018-0826-4](https://doi.org/10.1186/s40623-018-0826-4).

Okada, Y. 1985. "Surface Deformation Due to Shear and Tensile Faults in a Half-space." *Bulletin of the Seismological Society of America* 75 (4): 1135–1154.

Prats-Iraola, P., R. Scheiber, L. Marotti, S. Wollstadt, and A. Reigber. 2012. "TOPS Interferometry with TerraSAR-X." *IEEE Transactions on Geoscience and Remote Sensing* 50 (8): 3179–3188. doi:[10.1109/TGRS.2011.2178247](https://doi.org/10.1109/TGRS.2011.2178247).

Scheiber, R., and V. M. Bothale. 2002. "Interferometric Multi-Look Techniques for SAR Data." In *IEEE International Geoscience and Remote Sensing Symposium, Toronto, Canada*. Vol. 1, 173–175. IEEE.

Shan, X., G. Zhang, C. Wang, Y. Li, C. Qu, X. Song, L. Yu, and Y. Liu. 2015. "Joint Inversion for the Spatial Fault Slip Distribution of the 2015 Nepal M(w) 7.9 Earthquake Based on InSAR and GPS Observations." *Chinese Journal of Geophysics (In Chinese)* 58 (11): 4266–4276.

Shen, W., Y. Luo, and Q. Jiao. 2018. "Estimation of Static Coulomb Stress Change and Strong Motion Simulation for Jiuzhaigou 7.0 Earthquake Based on Sentinel-1 InSAR Data Inversion." *International Archives of the Photogrammetry, Remote Sensing and Spatial Information Sciences* 42: 3.

Small, D., C. Werner, and D. Nuesch. 1993. "Baseline Modelling for ERS-1 SAR Interferometry." In *International Geoscience and Remote Sensing Symposium, Tokyo, Japan* 1204–1206.

Sun, J., H. Yue, Z. Shen, L. Fang, Y. Zhan, and X. Sun. 2018. "The 2017 Jiuzhaigou Earthquake: A Complicated Event Occurred in A Young Fault System." *Geophysical Research Letters* 45 (5): 2230–2240. doi:[10.1002/grl.v45.5](https://doi.org/10.1002/grl.v45.5).

Tong, X., D. T. Sandwell, and Y. Fialko. 2010. "Coseismic Slip Model of the 2008 Wenchuan Earthquake Derived from Joint Inversion of Interferometric Synthetic Aperture Radar, GPS, and Field Data." *Journal of Geophysical Research: Solid Earth* 115 (B4). doi:[10.1029/2009JB006625](https://doi.org/10.1029/2009JB006625).

Wang, H., J. Wang, J. Yang, L. Ren, J. Zhu, X. Yuan, and C. Xie. 2018a. "Empirical Algorithm for Significant Wave Height Retrieval from Wave Mode Data Provided by the Chinese Satellite Gaofen-3." *Remote Sensing* 10 (3): 363. doi:[10.3390/rs10030363](https://doi.org/10.3390/rs10030363).

Wang, J., W. Yu, Y. Deng, R. Wang, Y. Wang, H. Zhang, and M. Zheng. 2019. "Demonstration of Time-Series InSAR Processing in Beijing Using a Small Stack of Gaofen-3 Differential Interferograms." *Journal of Sensors* 2019: 1–13. doi:[10.1155/2019/4204580](https://doi.org/10.1155/2019/4204580).

Wang, R., F. Diao, and A. Hoechner. 2013. "SDM - A Geodetic Inversion Code Incorporating with Layered Crust Structure and Curved Fault Geometry." In *EGU General Assembly Conference, Vienna, Austria* Vol. 15.

Wang, Y., W. Gan, W. Chen, X. You, and W. Lian. 2018b. "Coseismic Displacements of the 2017 Jiuzhaigou M 7.0 Earthquake Observed by GNSS: Preliminary Results." *Chinese Journal of Geophysics (In Chinese)* 61 (1): 161–170.

Werner, C., U. Wegmüller, T. Strozzi, and A. Wiesmann. 2000. "GAMMA SAR and Interferometric Processing Software." *Proceedings of the ERS-Envisat Symposium*, Gothenburg, Sweden 1620.

Wright, T. J., Z. Lu, and C. Wicks. 2003. "Source Model for the Mw 6.7, 23 October 2002, Nenana Mountain Earthquake (Alaska) from InSAR." *Geophysical Research Letters* 30 (18): 381–398. doi:10.1029/2003GL018014.

Wright, T. J. 2002. "Remote Monitoring of the Earthquake Cycle Using Satellite Radar Interferometry." *Philosophical Transactions of the Royal Society A: Mathematical Physical and Engineering Sciences* 360 (1801): 2873–2888. doi:10.1098/rsta.2002.1094.

Xie, Z., Y. Zheng, H. Yao, L. Fang, Y. Zhang, C. Liu, M. Wang, et al. 2018. "Preliminary Analysis on the Source Properties and Seismogenic Structure of the 2017 Ms 7.0 Jiuzhaigou Earthquake." *Science China Earth Sciences* 61 (3): 339–352. DOI:10.1007/s11430-017-9161-y.

Yang, Y., J. Fan, Q. Hua, J. Gao, C. Wang, L. Zhou, and T. Zhao. 2017. "Inversion for the Focal Mechanisms of the 2017 Jiuzhaigou M 7.0 Earthquake Sequence Using Near-field Full Waveforms." *Chinese Journal of Geophysics (In Chinese)* 60: 4098–4104.

Zhang, L., Q. Meng, S. Yao, Q. Wang, J. Zeng, S. Zhao, and J. Ma. 2018a. "Soil Moisture Retrieval from the Chinese GF-3 Satellite and Optical Data over Agricultural Fields." *Sensors* 18 (8).

Zhang, T., X. Lv, B. Han, B. Lei, and J. Hong. 2017a. "Repeat-pass SAR Interferometry Experiments with Gaofen-3: A Case Study of Ningbo Area." *arXiv Preprint arXiv:1704.01067*.

Zhang, X., W. Feng, L. Xu, and C. Li. 2017b. "The Source-process Inversion and the Intensity Estimation of the 2017 M(s) 7.0 Jiuzhaigou Earthquake." *Chinese Journal of Geophysics (In Chinese)* 60 (10): 4105–4116.

Zhang, Y., G. Zhang, E. A. Hetland, X. Shan, H. Zhang, D. Zhao, W. Gong, and C. Qu. 2018b. "Source Fault and Slip Distribution of the 2017 Mw 6.5 Jiuzhaigou, China, Earthquake and Its Tectonic Implications." *Seismological Research Letters* 89 (4): 1345–1353. doi:10.1785/0220170255.

Zhao, D., C. Qu, X. Shan, W. Gong, Y. Zhang, and G. Zhang. 2018. "InSAR and GPS Derived Coseismic Deformation and Fault Model of the 2017 Ms7.0 Jiuzhaigou Earthquake in the Northeast Bayanhar Block." *Tectonophysics* 726: 86–99. doi:10.1016/j.tecto.2018.01.026.